

# A Study of Bubble Behavior and Anode Effect on the Graphite and Industrial Carbon Anode in a See-Through Furnace During Aluminium Electrolysis



NIKOLINA STANIC, ANA MARIA MARTINEZ, KRISTIAN ETIENNE EINARSRUD,  
and ESPEN SANDNES

Anode gas bubble behavior and anode effect on graphite and industrial carbon rod-shaped anode in a cryolite melt have been studied using a see-through furnace. The different carbon materials have different properties which can affect bubble behavior and electrochemical properties. Industrial carbon is more inhomogeneous with respect to structure, pore, aggregates and impurities in comparison to the graphite. More bubbles were nucleated on the industrial carbon than on the graphite for the same current density. The time related to the coalescence process for both anodes was found to be in interval 16 to 24 ms and independent of the current densities. Bubbles detached from the horizontal surface of the anode have similar average diameter value for both anodes for current densities  $< 1.0 \text{ A cm}^{-2}$ , while for current densities  $> 1.0 \text{ A cm}^{-2}$ , the average diameter is lower for the industrial carbon anode. The onset of the anode effect occurred faster on the graphite than on the industrial anode. The PFC-containing gas layer appeared to be thicker and more stable on the graphite anode than on the industrial carbon anode.

<https://doi.org/10.1007/s11663-022-02583-6>  
© The Author(s) 2022

## I. INTRODUCTION

DURING the process of aluminum electrolysis  $\text{CO}_2$  gas bubbles are produced and released from the anode. Gas present at the anode surface contributes to an increase in cell voltage by covering the anode surface and reducing the active surface area which increases current density (hyperpolarization). Due to gas present at the surface, the current lines between the anode and cathode become prolonged causing so-called bubble overvoltage. The produced gas also causes an increase in ohmic resistance. The presence of bubbles makes an increase in energy consumption, the extra voltage drop due to bubbles is about 0.15 to 0.35 V out of a typical industrial cell voltage of  $\sim 4.5 \text{ V}$ .<sup>[1]</sup> Thus, increased knowledge about bubble behavior is important. The gas

evolution can be divided into three stages: nucleation, growth, and detachment. Bubbles nucleate at electrode surfaces, grow by mass transport of dissolved gas to the bubble surface or by coalescence with other bubbles, and detach from the electrode when forces pulling the bubbles away overcome the surface forces of adhesion. Many phenomena of gas evolution within each of these stages have been theoretically and experimentally investigated, but much remains to be studied in Hall-Héroult process.

Different carbon anode materials and anode surface properties affect bubble behavior. Huang *et al.*<sup>[2]</sup> studied bubble behavior under the graphite and industrial carbon anode in a transparent lab cell. Authors found that bubbles on the industrial anode just before release were larger in comparison to bubbles on the graphite anode in the current density interval 0.7 to 1.1  $\text{A cm}^{-2}$ . Gas coverage was found to be lower on industrial in comparison to a graphite anode. Bubble release period was found to be faster on the carbon than the graphite anode. Kasherman and Skyllas-Kazacos<sup>[3]</sup> studied the differences in the bath resistivity values for different anode materials, two carbon anodes with the same coke and pitch raw materials but with differences in granulation, the first had as authors referred optimum granulometry, while second had 50 pct fines fraction and was more porous than the first. The graphite was

---

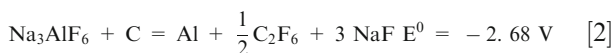
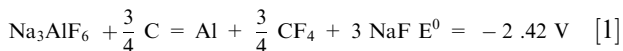
NIKOLINA STANIC, KRISTIAN ETIENNE EINARSRUD, and ESPEN SANDNES are with the Department of Materials Science and Engineering, Norwegian University of Science and Technology, NTNU, 7491 Trondheim, Norway. Contact e-mail: [nikolina.stanic@ntnu.no](mailto:nikolina.stanic@ntnu.no) ANA MARIA MARTINEZ is with the SINTEF Industry, 7034 Trondheim, Norway.

Manuscript submitted January 25, 2022; accepted June 11, 2022.

Article published online July 1, 2022.

also used as a third material. Different materials can influence the bubble contribution to the effective bath resistivity by affecting the nature of the CO<sub>2</sub> gas bubbles produced during electrolysis. The two most likely causes of this phenomenon are differences in bubble size and differences in wetting behavior of the anode materials. Kasherman and Skyllas-Kazacos results showed that the anode with non-optimized granulometry had a lower gas volume fraction and it would produce a smaller bubble contribution to the bath resistivity than first anode and graphite for bath with CR = 3. No current density data were reported. Thorne *et al.*<sup>[4]</sup> studied anodes made from differences in coke and a graphite anode. Isotropic cokes had higher level of impurities than anisotropic cokes. Anodes made of isotropic cokes showed slightly lower overpotential. In another study, Thorne *et al.*<sup>[5]</sup> observed from polarization curves that graphite operated at the higher potential in comparison to coke anodes. It was also found that anodes with lowest metallic and sulfur impurities had highest overpotential.<sup>[6]</sup> Metallic impurities could act as electrocatalyst, *i.e.*, to catalyze the anode reaction and therewith reduce overpotential.

An anode effect is a phenomenon in molten salts electrolysis, especially in aluminium electrolysis and is not well understood in detail. The anode effect is caused by depletion of alumina underneath the anodes and causes the resistance (and the voltage) to increase dramatically. In industrial cell the voltage can increase from around 4 V to as much as 40 V and even higher. As the anode effect occurs, the bottom operating surface of the anode seems to be entirely surrounded by a film of gas. This covers the surface of the anode and pushes the bath away, producing the so-called non-wetting of the anode. The anode effect causes low energy-efficiency and decreases the aluminium production of the cell. It also induces the formation of PFCs (CF<sub>4</sub> and C<sub>2</sub>F<sub>6</sub>) and increases formation of CO.<sup>[7]</sup> Thonstad *et al.*<sup>[8-10]</sup> studied anode effect on graphite anodes in cryolite-alumina melts prior to and during the occurrence of the anode effect by potential sweep and galvanostatic measurements. The onset for anode effect seems to be a depletion of oxygen-containing ions which is followed by co-deposition of fluorine that leads to anode effect. The anode surface is covered by insulating gas film that inhibits charge transfer. The film becomes thicker once anode effect is established. The insulating gas film contains (C-F) bond.<sup>[7]</sup> During anode effect the fluorine reacts with the carbon forming PFC gases, CF<sub>4</sub> and C<sub>2</sub>F<sub>6</sub>. PFC formation happens according to reactions<sup>[11]</sup>:



When a carbon anode in a molten salt is exposed to an increasing anode potential the current will eventually reach a so-called critical current density (ccd) and then abruptly dropped towards zero referring to an anode effect. Zhu and Sadoway<sup>[12,13]</sup> studied by cyclic

voltammetry and chronoamperometry mechanisms of electrode reactions on carbon anodes (microelectrode) and observed that anode effect occurred when the potential exceeds 3.4 V vs Al/Al<sup>3+</sup> the cell current drops precipitously for bath containing 0.4 wt pct Al<sub>2</sub>O<sub>3</sub>. It was observed that the existence of the resistive film formed on the anode surface was potential-dependent which means that the film can be formed and removed at will by regulation of applied potential. The exit gas during anode effect occurs contains a mixture of CO<sub>2</sub>, CO (secondary reaction between CO<sub>2</sub> and Al or C) and PFC gases (CF<sub>4</sub> and C<sub>2</sub>F<sub>6</sub>).<sup>[7]</sup> Tabereaux *et al.*<sup>[14]</sup> measured the change in the anode gas composition during anode effects in industrial cell and found that the gas mixture consists primarily of CO, 60 to 70 pct, and CO<sub>2</sub>, 20 to 30 pct; CF<sub>4</sub> content from both prebaked and Söderberg cells was in the range 16 to 20 pct, and the C<sub>2</sub>F<sub>6</sub> generation was small, 0.0 to 0.05 pct.

In previous work of Stanic *et al.*,<sup>[15]</sup> the see-through cell was used to study in detail bubble behavior on the horizontal and vertical graphite anode. The aim of the present work was to study bubble behavior on anodes made from different materials. Different carbon materials have different surface properties which can affect bubble behavior and electrochemical properties. One anode material was pure graphite and the other was industrial carbon. Graphite and industrial carbon show differences in composition (impurities content, *etc*), heterogeneity, porosity, surface roughness, *etc.*, that all have effect on bubble behavior (bubble life cycle, bubble size, wetting properties, *etc*). A shielded rod anode with defined surface area was used. The study goes into the details of bubble nucleation and its relationship with material surface properties. The bubble coalescence and size were studied for different current densities and discussed in detail. An additional focus of the study was on anode effects and how different materials affect it, prior to, during and after anode effect.

## II. EXPERIMENTAL

The experimental setup was the same as used in References 15, 16 and a principle sketch of the interior of the furnace is shown Figure 1. The furnace has two side openings which are closed with lids. In previous experiments lids were removed and replaced with quartz windows only during video recording in order to reduce heat loss. In this study when lids were removed, the furnace was left open during short recording times (max 60 seconds) in order to obtain clear images. The quartz crucible was resting at an alumina tower construction which was used to adjust the height level of the crucible. The alumina tower was resting inside and at the bottom of a ceramic crucible whose function was to catch the bath in case of crucible breakage during the experiment. Experiments were performed in a cryolite bath at a temperature of 890 ± 10 °C. The bath composition was synthetic cryolite with excess of AlF<sub>3</sub> equal to 24 wt pct and Al<sub>2</sub>O<sub>3</sub> concentration of 3 wt pct with addition of 15 wt pct LiF, 5 wt pct CaF<sub>2</sub>. The calculated liquidus temperature was 838 °C. Cryolite ratio was 1.85. It was

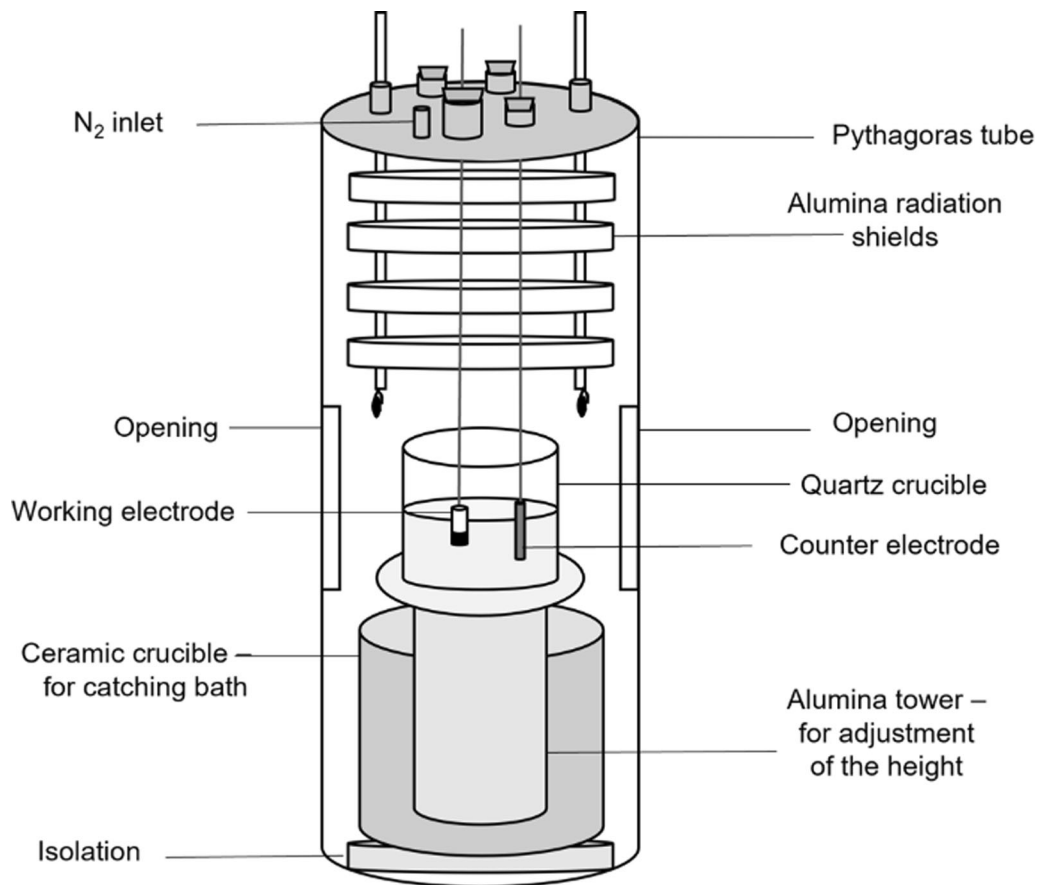


Fig. 1—Principle sketch of the interior of the furnace.

crucial to reduce the liquidus temperature this low to increase the service time of the quartz crucible. With the pure synthetic cryolite, (the liquidus temperature 1005 °C), the service time of the quartz crucible was that short that it was not practical to perform experiments. The superheat of  $\sim 50$  °C was on purpose kept this large in order to avoid bath freeze due to frequent openings of the furnace side lids. The bath was contained in the quartz crucible with a wall thickness of 2 mm.

An anode design used in this study was a shielded rod anode which has mixed geometry, *i.e.*, both horizontal and vertical surfaces, Figure 2. Two different types of carbon material were used, a purified graphite material (Schunk Tokai Scandinavia, AB, Sweden) and a sample from new industrial carbon anode (Hydro Aluminium AS Årdalstangen, Norway). Some physicochemical properties of the graphite and industrial carbon used for anode construction given by supplier are listed in Table I. A stainless steel (SS) rod with a diameter of 5 mm was used as a counter electrode, as in Reference [16]. The rod was immersed around 4 cm into the bath which gave an area of approx.  $6.5 \text{ cm}^2$ .

Electrochemical measurements were carried out using a PARSTAT (Princeton Applied Research) potentiostat and a 20 A KEPCO booster. A two-electrode system was used. A reference electrode was not applied due to space limitations in the cell and the object inside the bath made disturbance to the video image.

Electrochemical Impedance Spectroscopy (EIS) was used to determine the ohmic resistance of the cell at the Open Circuit Potential (OCP). OCP is the potential which the electrode obtains when it is not polarized. The electrolyte resistance  $R$  at OCP was used in the IR-compensation of the voltage-time data. IR-compensation is needed as a current passing through the electrolyte will always induce a voltage drop ( $IR$ ). Electrolysis was performed at constant current (in the interval  $0.1$  to  $2.0 \text{ A cm}^{-2}$ ) with a sampling frequency of 50 Hz. A linear sweep technique was used to study an anode effect. The sweep rate was deliberately chosen to be higher ( $5 \text{ V s}^{-1}$ ) in order to avoid many disturbances due to evolution of gas and to reduce convection to get clear and visible bath. The potential was swept from open circuit potential (OCP) to 10 V and video of reaction was recorded together with I-E data. Due to furnace/cell and camera limitations this was found to be an only way to obtain and observe an anode effect under the given conditions.

A Photron Fastcam Mini AX camera was used for the video recording. Different frame rates were used: 60, 500 and 1000 fps (frames per second). Photron Fastcam Viewer 4 (PFV4) software was used for controlling the Photron high-speed camera, for data saving, and for image processing. Potential  $\nu$ s time measurements were transformed into frequency spectra using a Fast Fourier Transform algorithm in “Sigview software-spectrum

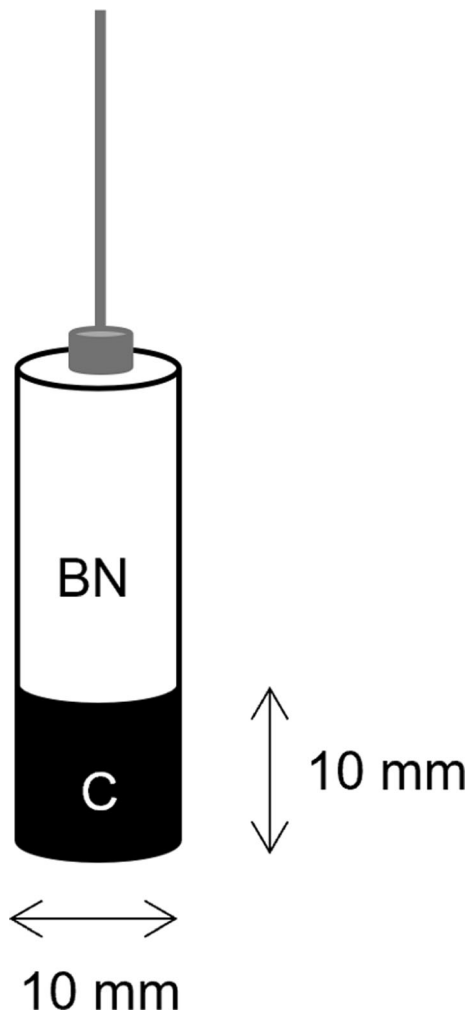


Fig. 2—The shielded rod anode with surface area  $3.9 \text{ cm}^2$ .

and signal analysis” using spectral analysis default settings.<sup>[17]</sup> The signals were transformed into the frequency domain to evaluate how the power of the signal is distributed over a range of frequencies to determine dominant frequency. The sampling rate ( $F_s$ ) was 50 Hz, consequently the spectrum has a frequency range from zero to  $F_s/2$ , 0 to 25 Hz. Dominant frequency is considered the frequency where FFT peak with the maximum magnitude of the signal is observed.

X-ray diffraction analysis was performed using a D8 A25 DaVinci X-ray Diffractometer with  $\text{CuK}\alpha$  radiation at room temperature (LynxEye™ SuperSpeed Detector). To perform analysis, anode material was ground to powder ( $< 250 \mu\text{m}$ ) and the powder was poured into a sample holder (5 mm deep, and 40 mm diameter). The sample holder was placed on the stage with the focusing plane of the X-ray tube. The scans were recording in the  $2\theta$  range between 5 and 90 deg with a scanning step 0.02 deg and accumulation time of 2 seconds. Total scanning time for one sample was 2h and 23 min. The indexing of the diffractions peaks was carried out using the powder database ICDD PDF-4 2021 by means of the card index PDF 00-056-0159C.<sup>[18]</sup>

X-ray computed tomography (CT) was used to investigate the structure and heterogeneity in samples. CT is a non-destructive technique that can represent the information visually at high resolution. One rod-shaped sample of graphite (L 300 mm) and one rod-shaped sample of industrial carbon (L 45 mm) both with a diameter of 20 mm that were used for an electrode construction, were sent to CT laboratory, MANULAB, NTNU Gjøvik for CT scanning using model Zeiss Metrotom 1500. For the scan, X-Ray tube was set for 90 kV and  $200 \mu\text{A}$ . Number of projection ( $N_p$ ) was 2050 (0.176 deg per projection). According to Villaraga-Gomez and Smith<sup>[19]</sup>  $N_p$  above 2000 is preferable for a satisfying accuracy of dimensional information provided by CT measurement. Although the rods are different length only  $\sim 20 \text{ mm}$  of the length of the sample was scanned. The basic unit in the CT image is the volume element, voxel (volumetric pixel). The CT image is composed of many voxels, depending on resolution and properties of the scanner, which are displayed as a 2D image array of picture elements (pixels). The voxel size of graphite material was  $13.85 \mu\text{m} \times 13.85 \mu\text{m} \times 13.85 \mu\text{m}$ , and voxel size of industrial carbon was  $12.83 \mu\text{m} \times 12.82 \mu\text{m} \times 12.83 \mu\text{m}$ . Picard *et al.*<sup>[20]</sup> observed that size of the sample affects the resolution of CT scan images and studied samples with 3 different diameter, 50.8 mm, 152.1 mm and 292.1 mm. Authors observed that aggregates and porosities were clearly visible in the smaller sample while they were not revealed in the larger one. The reason for this was that the voxel volume increases by increasing the sample size resulting in lower resolution. It is believed that size of graphite and industrial carbon rod (20 mm in diameter) used in present work for a CT analysis was sufficient to observe aggregates, impurities, and porosities.

### III. RESULTS AND DISCUSSION

#### A. Material Analysis

X-ray diffraction (XRD) analysis and Micro-computed tomography (micro-CT) of graphite and industrial carbon material were performed in order to analyze the crystallographic structure and macrostructure, respectively.

##### 1. Analysis of the graphite and industrial carbon by X-ray diffraction

Figure 3 shows X-ray diffraction patterns of the graphite and industrial carbon sample. The reflexes (002), (004), and (006) are reflections from stacked polyarene layers. Reflexes (004) and (006) are of higher order. The appearance of reflections (002) and its higher order reflections make it possible to calculate the crystallite size,  $L_c$ . For the graphite reflections (100) and (101) are less pronounced thus making the determination of  $L_a$  less accurate. Industrial carbon showed a smaller and broadened peak for the (002) reflection. The (100) band is also visible for the industrial carbon but no distinct peaks are visible. The same applies to the (110) band.

**Table I. Physicochemical Properties (from Supplier) of the Graphite and Industrial Carbon Used for Anode Construction**

	Graphite Anode	Industrial Anode
Density, g cm <sup>-3</sup>	1.80	1.60
Mean Aggregate size, μm	76	—
Electrical Resistivity, μΩm	10	52
Compressive Strenght, MPa	68.9	41.6
Ash Content, pct	< 0.6	0.25
Na, ppm	< 0.05	6
Al, ppm	< 0.08	11
Ca, ppm	< 0.04	42
Ni, ppm	< 0.1	170
Fe, ppm	< 0.04	160
Si, ppm	< 0.1	54
S	15 ppm	1.74 pct

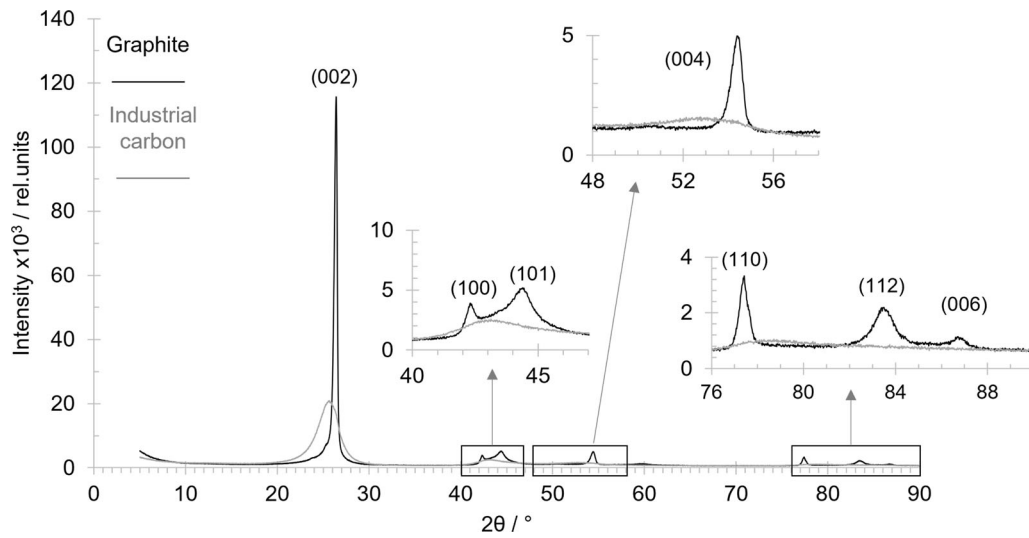


Fig. 3—X-ray diffraction patterns of graphite and industrial carbon.

The interplane distance ( $d_{002}$ ), structural components  $L_c$  and  $L_a$ , and the corresponding number of polyarene layers ( $N$ ), packing density of layers ( $\rho$ ), and degree of graphitization (D.G.), are calculated and results are given in Table II.

The interplanar distance,  $d_{002}$ , of the arene/graphene layers in the coherent domain is calculated using Bragg's law:

$$d_{00l} = \frac{\lambda}{2\sin\theta_{00l}}, \quad [3]$$

where  $\lambda$  is the radiation wavelength (1.5406 Å) and  $\theta$  is the reflection angle for the reflex 00l ( $l = 2, 4$  or  $6$ ).

The stacking height,  $L_c$ , is the dimension of the coherent domain perpendicular to the graphene plane. The crystallite size,  $L_a$ , is longitudinal dimension of the coherent domain.  $L_c$  and  $L_a$  are calculated using the Scherrer equation:

$$L = \frac{K\lambda}{\beta_{hkl}\cos\theta_{hkl}}, \quad [4]$$

where  $K$  is equal to  $\sim 0.9$  for C, and is a constant dependent on crystallite shape,  $\beta_{hkl}$  is the full width at half maximum (FWHM) of the reflex,  $\theta$  is the reflection angle for the reflex ( $hkl$ ), where  $hkl$  are Miller indices ((002) reflex and (100) reflex used for calculating  $L_c$  and  $L_a$ , respectively).

The number of polyarene layers,  $N$ , in the coherent domain is calculated:

$$N = \frac{L_c}{d_{00l}} + 1 \quad [5]$$

The packing density,  $\rho$ , of the layers in the coherent domain is calculated:

**Table II. Structural Parameters of the Graphite and Industrial Carbon**

Parameter	Graphite	Industrial Carbon
$2\theta$ , deg (002)	26.37	25.67
$d_{002}$ , Å	3.38	3.47
FWHM, deg (002)	0.41	2.77
FWHM, deg (100)	0.49	—
$L_c$ , Å	203	31
$L_a$ , Å	174	—
N	61	38
$\rho_{\text{bulk}}$ , g cm <sup>-3</sup>	1.80	1.60
$\rho_{\text{layer}}$ , g cm <sup>-3</sup>	2.24	2.18
p, pct	19.64	26.60
D.G., pct	70	—

$$\rho = \frac{3.354}{d_{00l}} \times 2.26, \quad [6]$$

where 3.354 (Å) is the interplanar distance ( $d_{002}$ ) in an ideal graphite crystal, and 2.26 (g cm<sup>-3</sup>) is the theoretical density of the ideal graphite.

Porosity,  $p$ , could be calculated:

$$p = 1 - \frac{\rho_{\text{bulk}}}{\rho_{\text{layer}}} \quad [7]$$

The degree of graphitization, D.G., can be roughly estimated using the equation<sup>[21]</sup>:

$$D.G. = \frac{3.44 - d_{00l}}{3.44 - 3.354}, \quad [8]$$

where 3.440 (Å) is defined the smallest interplanar distance in turbostratic carbon.

The interplanar distance  $d_{002}$  for the graphite material of 3.38 Å is well beyond the limit for turbostratic carbon and can definitely be termed a graphite. The industrial carbon has  $d_{002}$  of 3.47 Å which makes it a turbostratic carbon, but still a material with graphitic properties. Thus, from a crystallographic point of view the industrial carbon has more defects than graphite material. These findings make sense as the graphitization temperature producing the graphite (above 2000 °C) is much higher than the temperature during calcination of the coke (typically in the interval 1100 °C to 1300 °C).

*a. Estimation of the gas composition at low current densities based on XRD results and electrochemical measurements* Ouzilleau *et al.*<sup>[22]</sup> proposed an electrothermodynamic model for prediction of CO<sub>2</sub>/CO ratios. The model predicts that the CO<sub>2</sub>/CO ratio increases with the diameter of the coherent domain,  $L_a$ , of the coke. In the present work  $L_a$  for the graphite was found to be 17.4 nm. The  $L_a$  of industrial carbon was not calculated due to absence of the (100) reflex in the diffractogram (Figure 3). Due to the higher heat treatment temperature of the graphite than the

industrial carbon it can be assumed that  $L_a$  (ind. carbon) <  $L_a$  (graphite). Ouzilleau *et al.*<sup>[22]</sup> proposed the use of a  $L_a/L_c$  ratio of 1.35 for typical industrial carbon. From this ratio and the calculated  $L_c$  for the industrial carbon anode (Table II),  $L_a$  is estimated to 4.2 nm. The model predicts that the graphite anode should give higher CO<sub>2</sub>/CO ratio above the reversible potential for CO<sub>2</sub> evolution.

Ouzilleau *et al.*<sup>[22]</sup> compared data from the model with CO<sub>2</sub>/CO ratios measured by Thonstad<sup>[23]</sup> and Drossbach.<sup>[24]</sup> The model was plotted based on conditions used by Drossbach, temperature 890 °C and alumina concentration close to saturation and estimated  $L_a$  to be 3 ± 0.5 nm. These conditions are similar to the conditions of the present work concerning the industrial carbon anode. Assuming the cathodic overvoltage is very low at lower current densities (0.1 A cm<sup>-2</sup>) the cell voltage approx. equals the anode potential which normally would be measured versus aluminium reference electrode. For the current density of 0.1 A cm<sup>-2</sup>, the cell voltage was 1.02 V when using the graphite anode and 0.9 V when using the industrial carbon. Using these voltages and the model results for 890 °C and alumina saturation, a CO<sub>2</sub>/CO ratio less than 1 is found from the model. This means that CO is likely the major product on the anode at this low current density.

For the current density of 0.25 A cm<sup>-2</sup>, the corresponding voltage at the beginning of electrolysis was found to be around 1.25 V for the industrial carbon. From this the model predicts CO<sub>2</sub>/CO ratio to be 4. The ratio increases rapidly with anode potential. Therefore it could be assumed that in the current work images that show bubbles produced at the current density 0.1 A cm<sup>-2</sup> mostly represents CO while for the current density ≥ 0.25 A cm<sup>-2</sup> a major fraction of produced bubbles is CO<sub>2</sub>.

The difference in cell voltage of 0.12 V at 0.1 A cm<sup>-2</sup> when using the graphite and the industrial carbon anode can be explained with the findings of Ouzilleau *et al.*<sup>[22]</sup> who observed reversible anode potential decreases with decreasing  $L_a$ . Ouzilleau *et al.* calculated potential at 1273 K and 1 atm for different coke crystallites. Since the industrial carbon has a lower  $L_a$  than the graphite anode, *i.e.*, 4.2 < 17.4 nm, it is expected that the reaction on the industrial carbon proceeds at a potential lower than for the graphite.

## 2. Micro X-ray computed tomography (CT)

Figures 4 and 5 show CT images of the cross section of the graphite and industrial carbon material. On the CT images of the graphite (Figure 4) it can be seen that the structure is rather homogeneous in comparison to the industrial carbon. No larger pores were observed. White spots, representing regions of high density, were observed to appear and disappear when scanning through sample. Picard *et al.*<sup>[20]</sup> studied prebaked carbon anode using CT and observed that impurities were represented by white spots on the CT images. The outer edge appears to be even indicating a smooth surface. CT images of the industrial carbon, Figure 5, show variety in the structure. The material is made of coke aggregate of different sizes bonded together by the

pitch coke formed during baking. The aggregates cannot generally be distinguished, the structure is more sponge coke like, sponge coke being the typical coke preferred by anode producers. The pores are within the sponge coke and between aggregates. The largest aggregate particle was found to have width in x-y direction and height in y-z direction of approx. 5 and 3 mm, respectively. The first appears in image 9 in Figure 5, while in image 10 it is close to its maximum width. In image 11 it has already disappeared. Similar numbers for the pores were approx. 2 mm width and 3 mm depth. Only one industrial carbon sample was analyzed, thus not necessary represents the situation for the whole industrial anode it was taken from.

Figure 6 shows enlarged upper part of the CT images for more detailed presentation, image 2 from Figure 4 for the graphite and image 2 from Figure 5 for the industrial carbon. For the graphite in Figure 6(a), aggregates can be observed (lighter in color) with the darker binder phase in between them. Aggregates are different in size, *i.e.*, majority of the aggregates have width less than 100 microns, while a few have width up to 300 microns. The supplier stated an aggregate average value to be 79 microns, Table I. In Figure 6(b) on the industrial carbon sample pores, cracks and sponge coke can be easily observed. Coke aggregates lighter in color can be also observed although they are not so distinct,

possibly due to similar density as the pitch. As mentioned above white spots for both samples are probably impurities.

It can be observed that the graphite anode has a smoother outer surface without cracks and pores compared to the industrial anode. The effects of the cracks and pores on the bubble behavior (bubble nucleation, bubble layer, *etc*) are discussed in relation to the images from the see-through cell discussed below.

### 3. Potential-time data

Figure 7a) shows cell voltage-time data for both graphite and industrial carbon anode at  $1.0 \text{ A cm}^{-2}$ . Potential oscillation has characteristic saw-tooth shape studied in detail in References 25 and 26. As can be seen the saw-tooth curve and voltage drop for the graphite and industrial carbon anode is different although the average bubble size (in 3.3.3) is similar for both anodes for the same applied current. The cell voltage appears to be similar too. The experiment was not designed to study potential difference for anodes made of different material and the cell voltage is not discussed. The saw-tooth curve is representing one big bubble cycle.<sup>[15,25,26]</sup> The voltage drop occurs when bubble detaches. The lowest value of voltage represents a surface free from big bubbles. New smaller bubbles are produced and the voltage is rising. Bubbles are growing and coalescing into one big bubble that will eventually

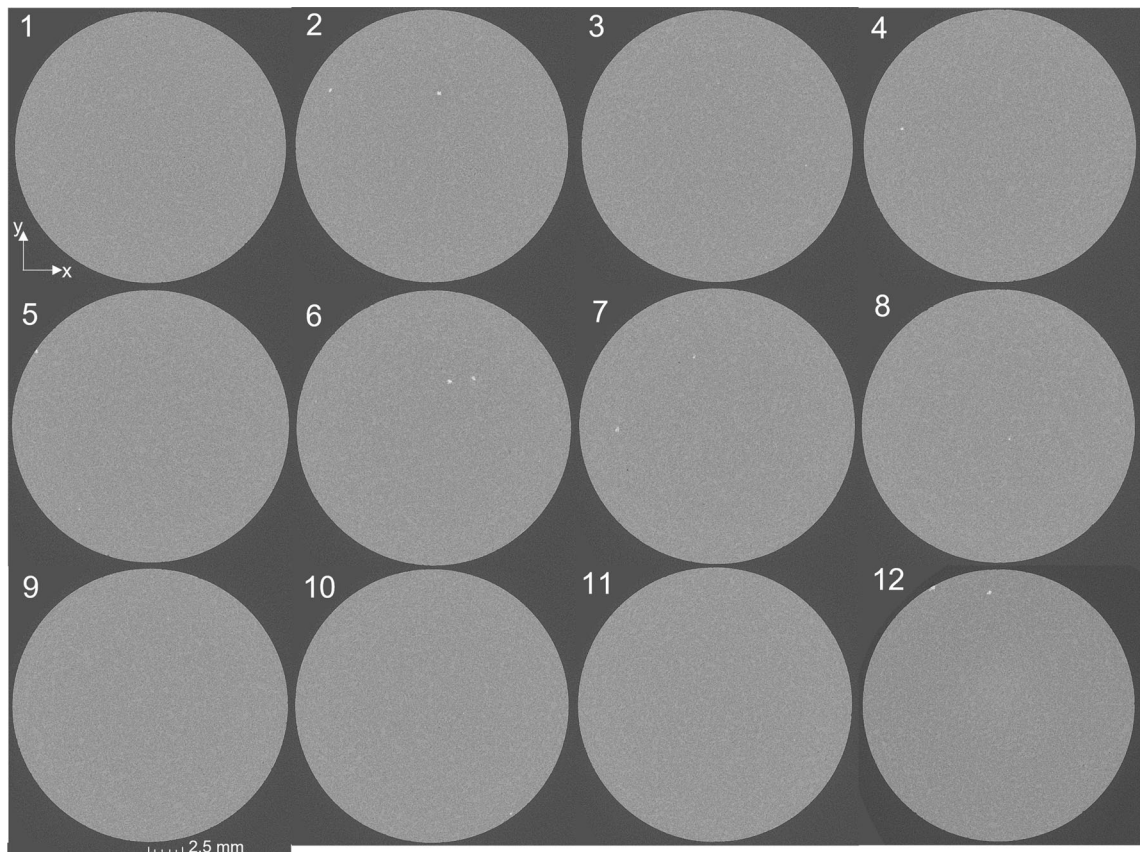


Fig. 4—CT images of the cross section of the graphite rod sample ( $\text{Ø } 20 \text{ mm}$ ). The distance between each image is 1.87 mm. The figure therefore shows the graphite rod sample over a length of 20.57 mm. Orientation axis are shown in image 1. Images lie in x-y plane.

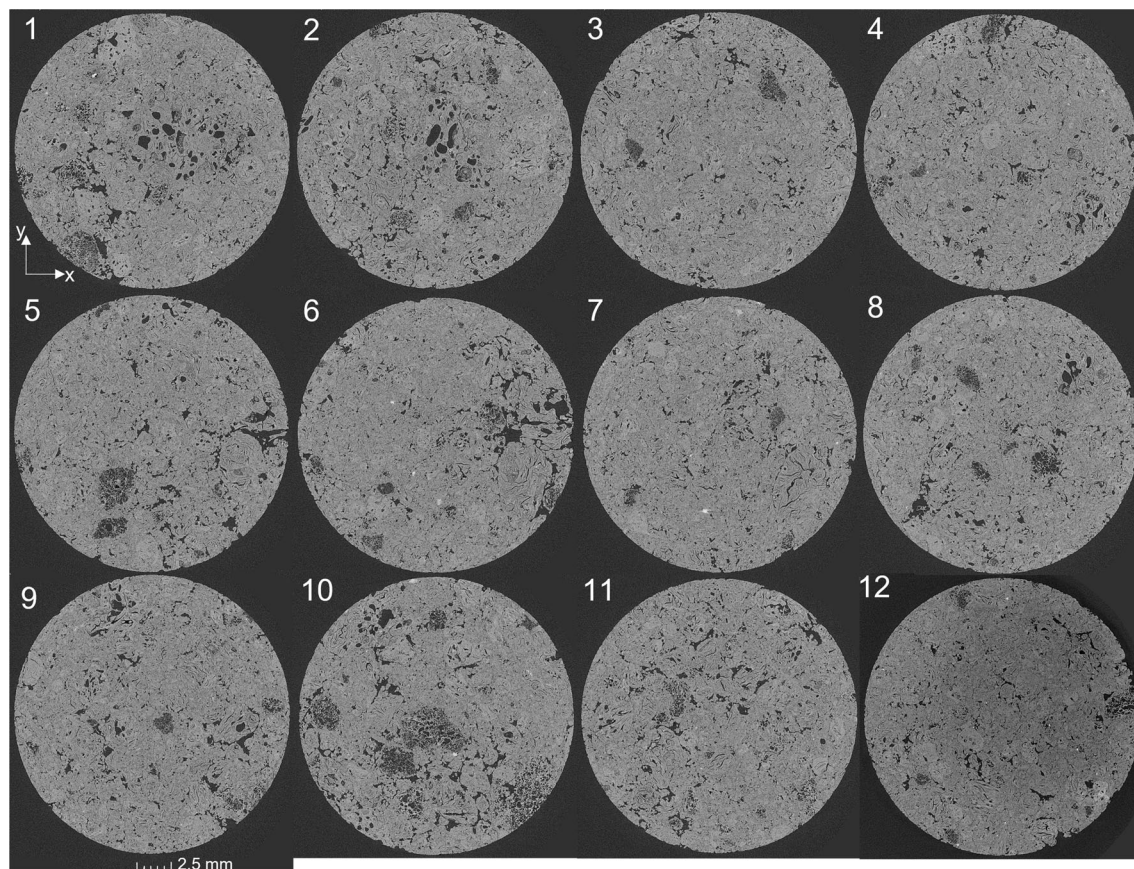


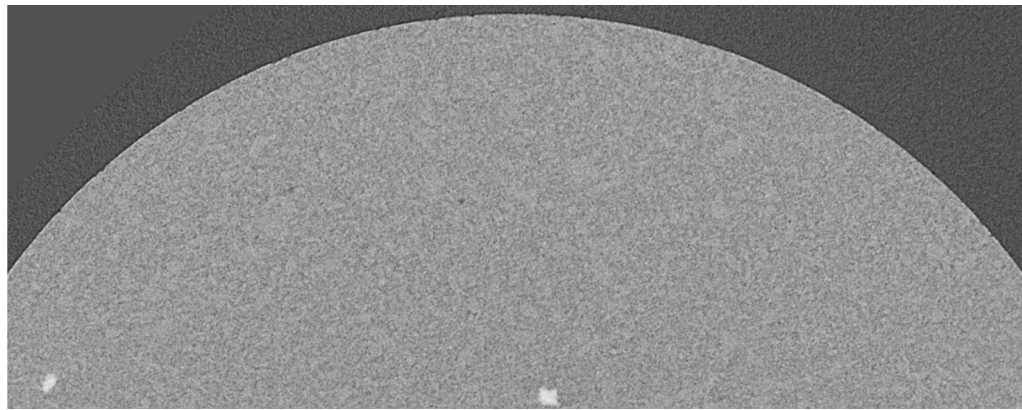
Fig. 5—CT images of cross section of the industrial carbon rod sample ( $\text{\O} 20 \text{ mm}$ ). The distance between each image is 1.99 mm. The figure therefore shows the industrial carbon rod sample over a length of 21.89 mm. Orientation axis are shown in image 1. Images lie in x-y plane.

be detach and the voltage drop will occur again. Bubbles from the vertical side does not contribute much to the oscillation since the oscillations are very small.<sup>[25]</sup> The bubbles responsible for the oscillations at the saw-tooth curves are all events happening at the horizontal surface, *i.e.*, bubbles nucleation, growth, coalescence, sliding, *etc.* In video recordings it was observed that at the industrial carbon anode for current densities  $\geq 1.0 \text{ A cm}^{-2}$  in addition to a big bubble detaching from the horizontal part of the anode, smaller bubbles, were also sometimes formed and detached from the horizontal anode edge. The formation and detachment of smaller bubbles at the anode edge increases with increasing current density. These bubbles are larger than bubbles formed and detached at the vertical side of the anode. Since the anode is observed from only one side and horizontal part of the anode is not seen in total from below it is believed that those individual smaller bubbles could exist at all over the edge of the horizontal surface and when the big bubble is sliding towards the anode edge to be detached it withdraws other bubbles on its path and all are together detached. The voltage drop is larger for the industrial carbon anode than for the graphite anode. From the video recording, it was observed that a bubble coverage of the industrial anode is higher than on the graphite anode. The industrial

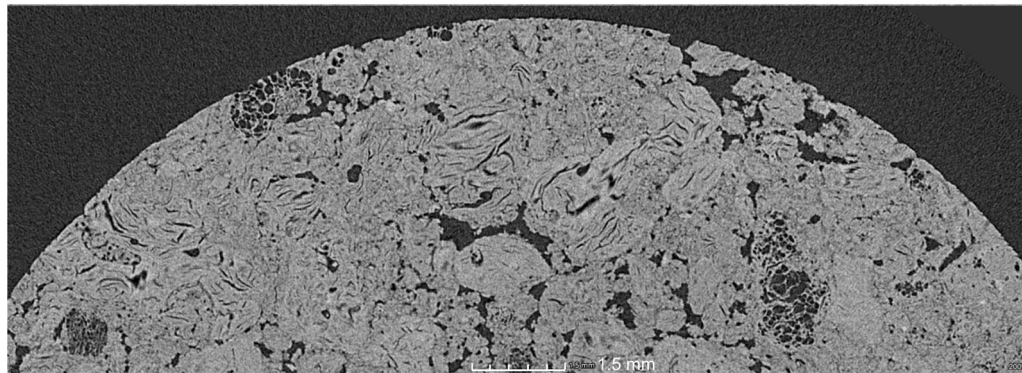
carbon anode has more active surface and the nucleation is more powerful which lowers the voltage additionally. On the graphite anode nucleation is slower and needs more driving force. The rise in the voltage after voltage drop, *i.e.*, bubble detachment, is sharper for the industrial carbon than the graphite anode. This could also be explained with the nucleation that happens faster at the industrial carbon anode and smaller bubbles coalesced into one big bubble that grow faster and is detached. As discussed below, the number of nucleation sites is larger for the industrial carbon and more bubbles are formed at the same current density in comparison to the graphite anode. On the horizontal side of the anode more bubbles were formed and detached from the industrial carbon anode.

Fast Fourier transform analysis (FFT) of the cell voltage-time data for both anodes at  $1.0 \text{ A cm}^{-2}$  is shown in Figure 7(b). For the graphite and industrial carbon anode a dominant FFT peak is observed at 0.15, and at 0.27 Hz, respectively. This dominant peak frequency probably corresponds to a bubble detachment time for the bubble from the horizontal part of the anode.<sup>[15,25]</sup> The life cycle of one big bubble on the horizontal surface is shorter for the industrial carbon anode in comparison to the graphite anode.





(a)



(b)

Fig. 6—Enlarged upper part of the CT images; (a) image 2 from Figure 4 (graphite sample) (b) image 2 from Figure 5, (industrial carbon sample).

## B. Bubble Properties and Bubble Dynamics

### 1. Bubble nucleation and bubble development

Figure 8 shows anode surface area of the rod anode for the graphite and industrial carbon anode during electrolysis at constant current of  $0.1 \text{ A cm}^{-2}$  at different times from the beginning of electrolysis  $\sim 6$ ,  $\sim 14$  and  $\sim 21$  seconds. For both anodes it was observed that bubbles were nucleated at certain nucleation sites on the anode surface for the same current density, but nucleation was more pronounced for the industrial carbon than graphite, *i.e.*, relatively more bubbles were formed and detached from the industrial carbon for the same current density. This is due to differences in surface heterogeneity in relation to CT a structure of coke and possible different composition wrt. to metallic impurities and sulfur. The quantity of the nucleation sites depends on the structure of the anode. Classical nucleation theory predicts a reduced energy barrier in surface defects.<sup>[27]</sup> Nucleation takes place on active sites which are defects and pores on the anode surface. As can be seen in the CT images (Figures 4 and 5) the industrial carbon has larger surface irregularity compared to the graphite anode. In other systems this phenomenon was also found, *e.g.*, Westerheide and Westwater<sup>[28]</sup> studied isothermal growth of hydrogen bubbles during electrolysis at a platinum cathode and reported that nucleation

occurred at specific nucleation sites being preferred as pits and scratches which acted as active sites on the electrode.

Bubble evolution over time is shown in Figure 8. As discussed in previous work,<sup>[15]</sup> after immersing the anode in the bath, non-electrochemical bubbles are formed and sticking at both boron nitride and graphite/industrial carbon part. After electrolysis started, non-electrochemical bubbles were removed by electrochemical bubbles, *i.e.*, gaseous reaction products. Since it took  $\sim 5.5$  s from the beginning of the electrolysis for all nonelectrochemical bubbles to be removed from the anode surface, the frames in Figure 8 shows only gas products. Between 14 and 21 seconds a big bubble is detached from the horizontal surface of the industrial carbon anode. At  $\sim 21$  seconds at the left vertical sides of the industrial carbon anode it seems like bubbles are accumulating at the surface, something like “bubble foam” occurred. Produced bubbles are not big enough to be detached and the effect of the bubble-induced convection and current is not enough to promote bubble detachment. In some point bubbles will grow and coalesce and be detached from the surface. In this specific case accumulation of bubbles didn’t occur at the right vertical side of the anode. The reason is that the big bubble from the horizontal side was latterly detached at

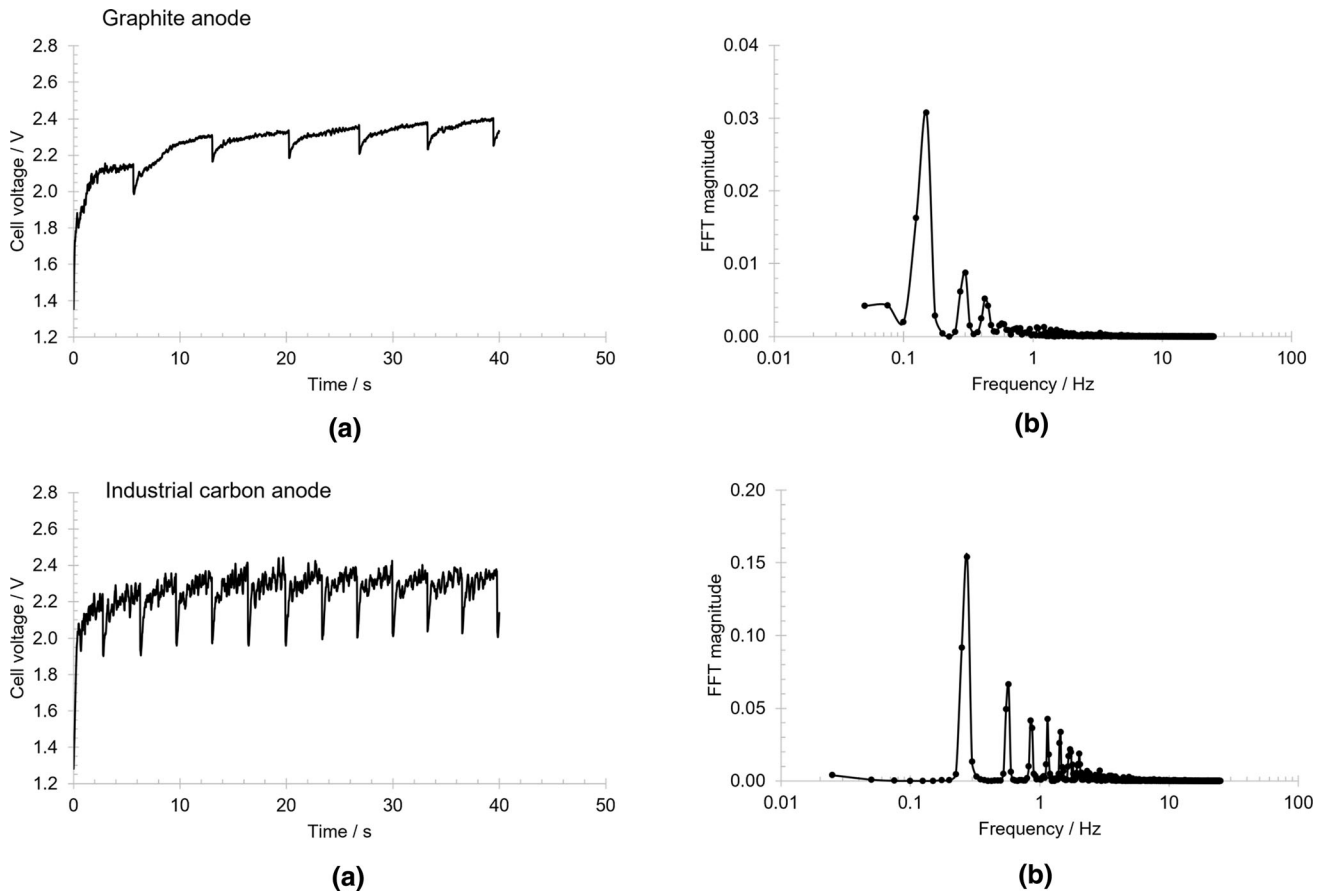


Fig. 7—(a) Cell voltage-time data for the graphite anode and industrial carbon anode during electrolysis at constant current density of  $1.0 \text{ A cm}^{-2}$ . Cell voltage data are post-IR-compensated. (b) FFT spectra of cell voltage-time data for the graphite and industrial carbon anode.

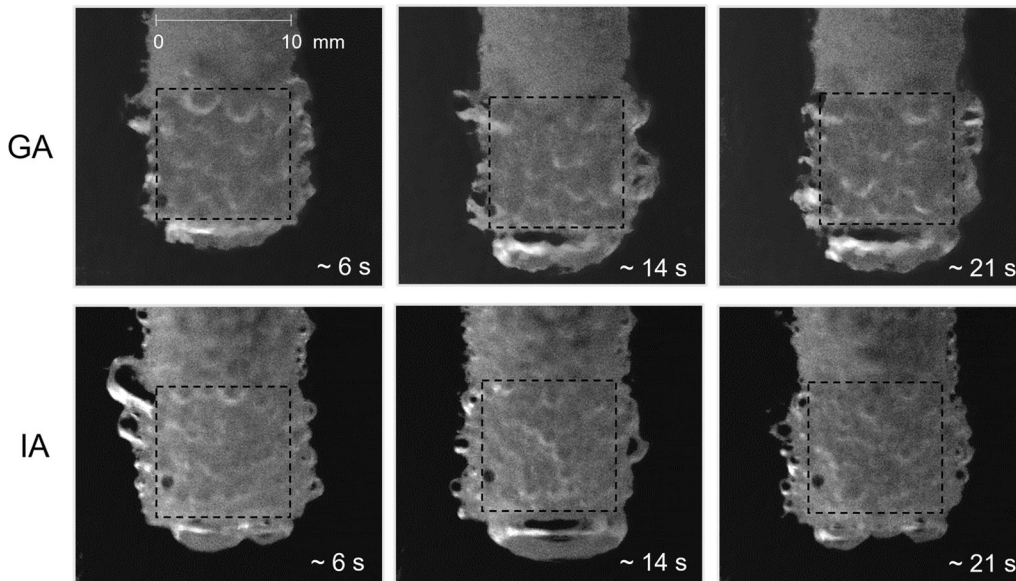


Fig. 8—Anode surface area (the black dashed line illustrating the border of the anode surface) of shielded rod anode for graphite (GA) and industrial anode (IA) during electrolysis at constant current of  $0.1 \text{ A cm}^{-2}$ . The time stamps refer to the time after start of electrolysis. The capture frame rate was 500 fps. A scale bar is shown.

the right side and while rising up it withdrew some smaller bubbles from the vertical side which otherwise

would not yet be detached. The process is shown in Figure 9. The occurrence of the “bubble foam”

phenomenon was not observed for the graphite anode. It was observed that nucleation points were more or less at the same position for the graphite anode for observed time. For the industrial anode more bubbles are formed with time despite current remaining constant.

Figure 9 shows a big bubble sliding along the horizontal surface towards the anode edge, frames (1) and (2), and its detachment, frame (3). While rising up, frame (4), the big bubble entrains smaller bubbles from the vertical surface and making them to detach, leaving the surface free of bubbles, frames (5) to (8). The process was observed for both anodes.

## 2. Dynamics of the gas bubble coalescence

Coalescence was studied for both anodes for different fps and different current densities. High fps was used in to order to capture formation of the intermediate. Bubble coalescence is a process by which two or more gas bubbles in a liquid medium collide and form one larger bubble. Coalescence occurs in three stages: *i.e.*, collision of particles, drainage of the film of liquid during the collision and later film rupture leading to a larger bubble. In previous study of vertical graphite anode<sup>[15]</sup> it was found that coalescence process occurred in time interval of 16 to 20 ms and that the current density and electrode potential did not have a significant influence on the time for the coalescence process. In the present study it was also observed at video recorded with 500 fps and 1000 fps that coalescence process for both anodes lie in interval 16 to 24 ms for current densities 0.1, 0.25 and 0.5 A cm<sup>-2</sup>. In Figures 10 and 11, coalescence processes are shown on the vertical surface for both anodes, for current densities where images with the best visibility were obtained. Corresponding videos of the coalescence processes on the graphite anode and

the industrial carbon anode can be found in the electronic supplementary material, ESM 1 and ESM 2, respectively. In Figure 12 is shown process of coalescence at the horizontal surface for the graphite anode. The corresponding video is available in the electronic supplementary material ESM 3.

Figure 10 shows the coalescence process of two bubbles (highlighted with white dashed line) into one bigger bubble at the vertical surface of graphite anode during electrolysis at a constant current density of 0.1 A cm<sup>-2</sup>. Frame (1) is believed to be a frame where gas bubbles came in touch and “collision” of gas bubbles and drainage of the film occurred. In frames (17–21) are shown film rupture and formation of one larger bubble. The total time of the process was found to be 21 milliseconds.

Figure 11 shows the process of coalescence of two bubbles (highlighted with white dashed line) into one bigger bubble at the vertical surface of industrial anode during electrolysis at a constant current density of 0.25 A cm<sup>-2</sup>. Frame (1) is believed to be a frame where gas bubbles came in touch and “collision” of gas bubbles and drainage of the film occurred. Frames (8) to (12) show the film rupture and formation of one larger bubble which detached immediately (frame 13) from the anode surface. The total time of coalescence process was found to be 22 ms.

The process of coalescence of two bubbles into one bigger bubble at the horizontal surface of the graphite anode during electrolysis at a constant current density of 0.1 A cm<sup>-2</sup> is shown in Figure 12. Since observation is made from the side it is difficult to state when exactly the process of coalescence starts but it is believed that coalescence occurred in the interval 16 to 24 ms as was found for the bubbles on the vertical side. Two bubbles

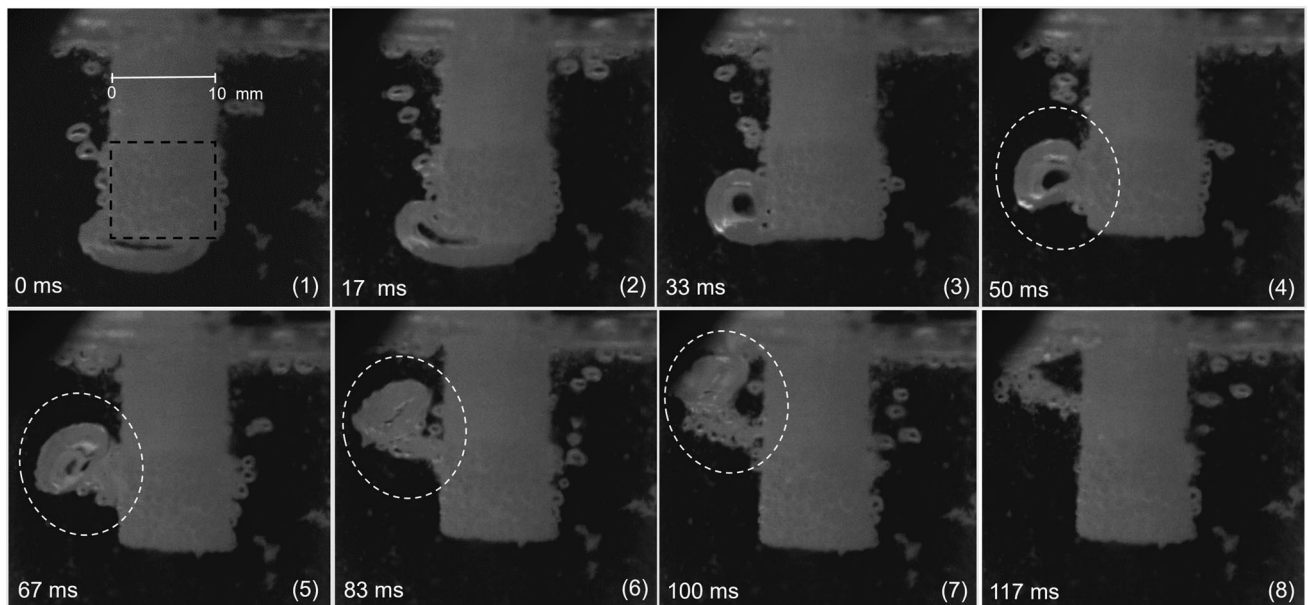


Fig. 9—Big bubble (highlighted with white dashed line) while detaching from the horizontal surface of the graphite rod anode withdraws smaller bubbles from the vertical surface at 1.0 A cm<sup>-2</sup>. Border of the anode surface area is highlighted with black dashed line. The frame rate was 60 fps. Frame numbers are given in brackets. Timestamp of 0 ms is added to frame (1), by that, other frames are relative to the first frame. A scale bar is shown in frame (1).

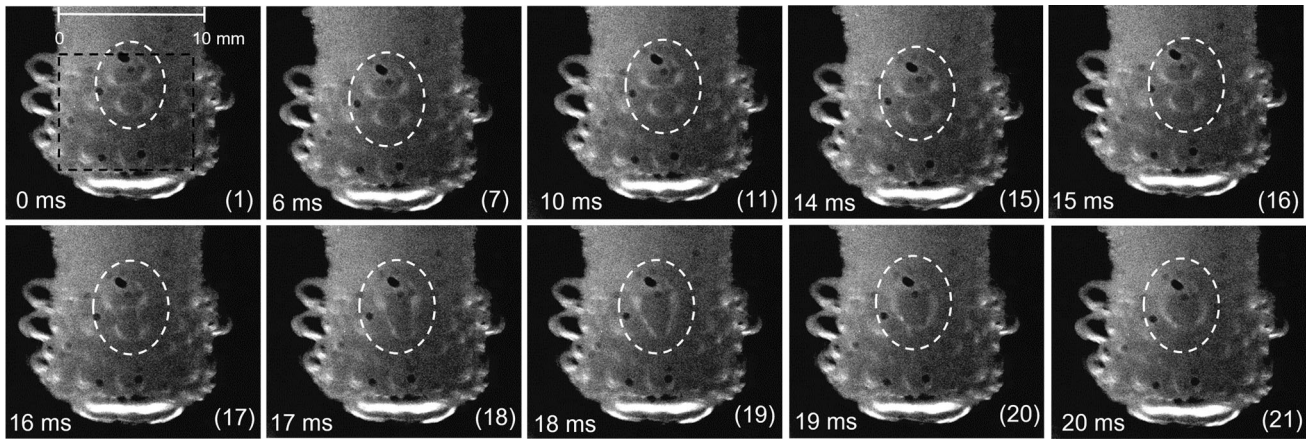


Fig. 10—The process of coalescence of two bubbles (highlighted with white dashed line) into one bigger bubble at the vertical surface of graphite anode during electrolysis at a constant current density of  $0.1 \text{ A cm}^{-2}$ . Frame (1) represents the beginning of the coalescence process and is given a 0 ms timestamp, by that, other frames are relative to the first frame. The frame rate was 1000 fps. The anode surface is highlighted with a black dashed line in frame (1) together with a scale bar.

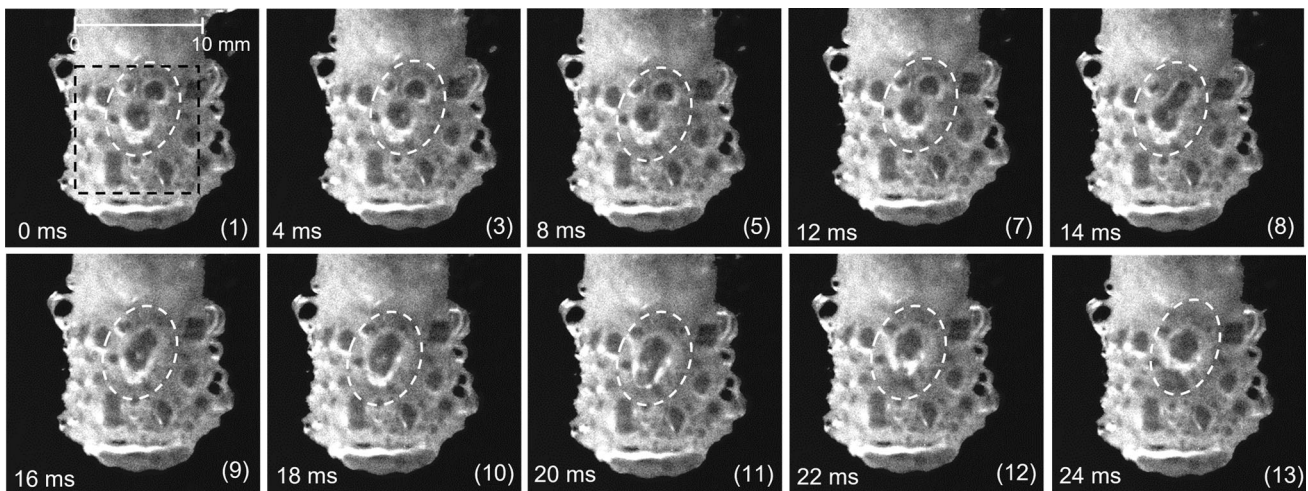


Fig. 11—The process of coalescence of two bubbles (highlighted with white dashed line) into one bigger bubble at the vertical surface of industrial anode during electrolysis at a constant current density of  $0.25 \text{ A cm}^{-2}$ . Frame (1) represents the beginning of the coalescence process and is given a 0 ms timestamp, by that, other frames are relative to the first frame. The frame rate was 500 fps. The anode surface is highlighted with a black dashed line in frame (1) together with a scale bar.

collided and film rupture happened at frames (1 to 3) and intermediate is formed, frames (4 to 6). A resulting big bubble was spread all over horizontal surface, frames (7 to 11). The bubble slid towards the anode edge, but did not detach, frame (16). As seen in frame (19), the bubble was centered at the horizontal surface and took nearly spherical shape. The bubble tended to be pulled into a spherical shape due to greater forces between the graphite and electrolyte. The bubble continued to grow covering majority of the anode surface and with thus removing electrolyte from the surface. After the bubble grew to a certain size it reached the edge and detached from the surface. The same bubble behavior was observed for the industrial carbon anode. Values for wetting angle of the bubble at the horizontal surface just before its detachment was measured to be in the interval 110 to 125 deg for both anodes during

electrolysis at  $0.1 \text{ A cm}^{-2}$ . The wetting angle was determined by drawing a tangent to the bubble profile at the point of the three-phase contact on an image.

### C. Bubble Size

The average bubble diameter after bubble detachment from the graphite and industrial anode as a function of current density is presented in Figure 13. Error bars represent a 95 pct confidence interval assuming a normal distribution. The bubble diameter was calculated as an average value of 10 bubbles detached from horizontal surface and an average value of 15 bubbles detached from vertical surface at each current density. The bubble diameter was measured using PFV4 software as explained by Stanic *et al.*<sup>[15]</sup> The bubble diameter values in Figure 13 are from several different

experiments. The bubble diameter decreases with increasing current density, but with a different rate for different materials. For the graphite anode, diameter of the bubbles from the horizontal part has an average value of 7.5 mm and is reduced to 6.7 mm at  $0.5 \text{ A cm}^{-2}$  wherefrom it stays nearly constant up to  $2.0 \text{ A cm}^{-2}$ . For the industrial carbon anode, diameter of the bubbles from the horizontal part has an average value of 7.5 mm and is reduced to 6.7 mm at  $0.8 \text{ A cm}^{-2}$  while from  $1.0 \text{ A cm}^{-2}$  decrease in average value is more pronounced (to 4.5 mm at  $2.0 \text{ A cm}^{-2}$ ) and with a higher standard deviation. For the industrial carbon anode above  $1 \text{ A cm}^{-2}$ , a larger variance was observed in detached bubble diameter from horizontal surface. At the horizontal part of the anode close to the anode edge, smaller bubbles that were formed there were detached without coalescing with the big bubble growing in the middle of the horizontal anode surface, *i.e.*, edge effect. Those bubbles grown to certain size, 2.5 to 3.5 mm, and are detached. Simultaneously in the middle of the anode

a big bubble is growing and while reaching certain size (larger than bubbles from the edge), slides toward the edge and is detached. This edge effect was not observed for the graphite anode. Contrary at the graphite anode above  $1 \text{ A cm}^{-2}$  average bubble diameter is more or less constant.

Bubbles from the vertical surface are found to be similar in size for both anodes, Figure 13. It is believed that at lower currents bubble retention time is higher and bubbles have time to grow and coalesce more while at higher currents more bubbles are formed and their retention time is shorter, *i.e.*, already existing bubbles are rapidly pushed by newly produced bubbles. Bubble-induced convection also contributes bubble release and is larger with increasing current.<sup>[29]</sup> Results indicate that anode material also affects bubble size along with already discussed current density and convection. Industrial carbon has more variety in surface in comparison to graphite anode and greater number of nucleation sites. Due to larger variation in surface on the industrial carbon material, as discussed in Section III-A-2, one

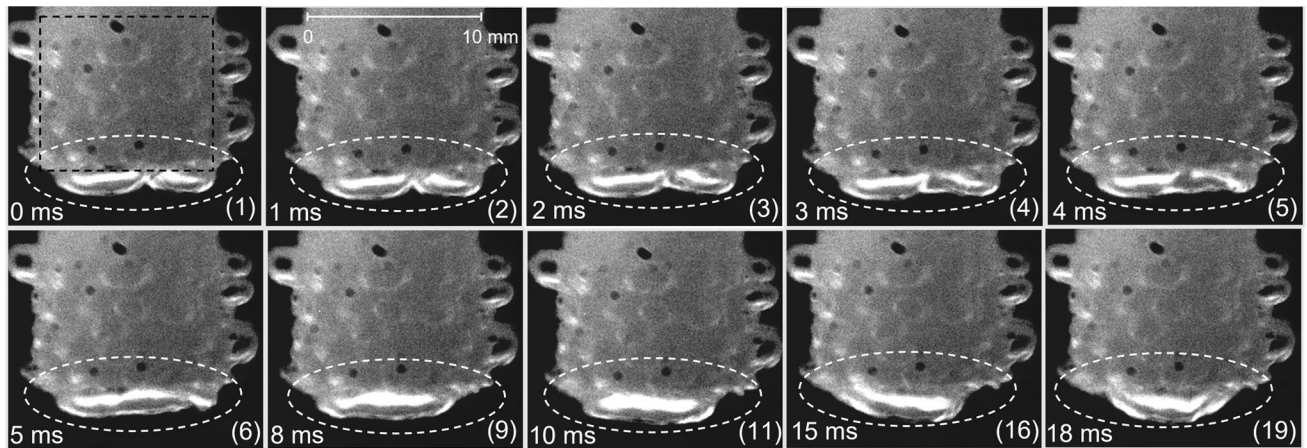


Fig. 12—The process of coalescence of two bubbles (highlighted with white dashed line) into one bigger bubble at the horizontal surface of the graphite anode during electrolysis at a constant current density of  $0.1 \text{ A cm}^{-2}$ . Frame (1) represents the beginning of the coalescence process and is given a 0 ms timestamp, by that, other frames are relative to the first frame. The frame rate was 1000 fps. The anode surface is highlighted with a black dashed line in frame (1) together with a scale bar, frame (2).

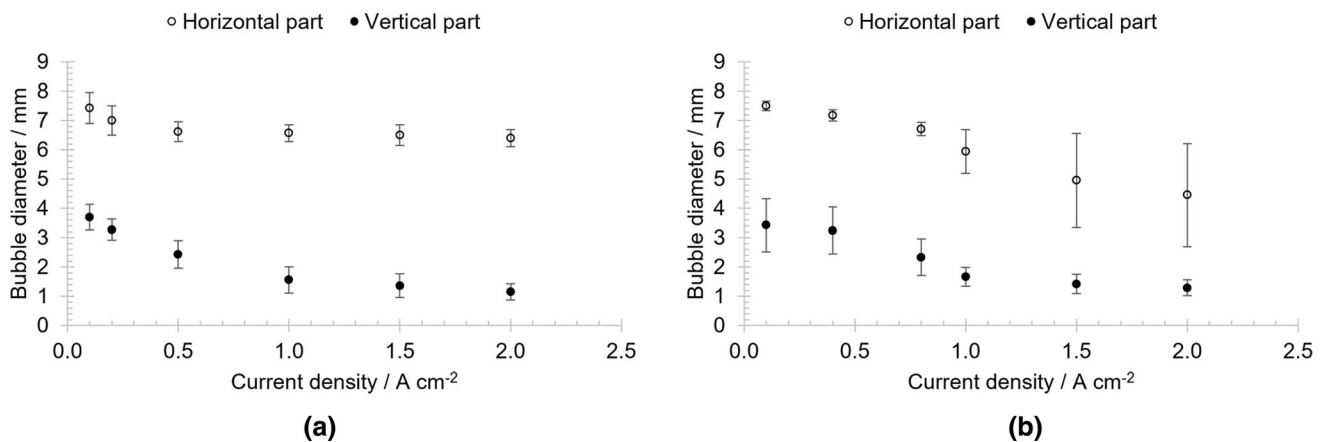


Fig. 13—Bubble diameter from horizontal and vertical part of anode for the (a) graphite anode and (b) industrial anode as a function of the nominal current density.

cannot conclude how some other anode made from the same industrial carbon material would behave. Bubble accumulation at the vertical side over time on the industrial carbon anode (discussed in 3.3.1) is believed to be favored by lower current densities, while at higher current densities bubble accumulation is less pronounced. This is confirmed by obtaining the nearly constant value in bubble diameter above  $1.0 \text{ A cm}^{-2}$ .

As explained in our previous study,<sup>[15]</sup> the increase in current density and thereby the corresponding increase in potential gives higher driving force for nucleation of relatively more bubbles. Cassayre *et al.*<sup>[30,31]</sup> also found that the bubble diameter decreased with increasing current density. It was explained by less pronounced coalescence at higher current densities and that bubbles escape before covering the anode and grow to full size.

Images of bubbles at the same graphite anode for different current densities can be seen in Figure 14. All images are taken at the same event in the bubble cycle, *i.e.*, the big bubble from the horizontal surface is sliding toward the anode edge (a), the big bubble is detaching from the anode edge (b) and the big bubble is leaving the surface (c).

#### 1. Current density at the horizontal part of the anode

The volume of each bubble detached from the horizontal surface was calculated using the equation for the volume of a sphere since it was observed that after detachment bubbles in one moment had a spherical shape. Knowing the total number of detached bubbles and their diameter the total gas volume produced at the horizontal surface was calculated and results are shown in Figure 15(a). To get a volume fraction of gas produced at the horizontal surface, this value was divided with the total gas volume produced at the rod anode according to Faraday's law assuming even current distribution and  $\text{CO}_2$  as the only gaseous product. In the current density interval  $0.4$  to  $2.0 \text{ A cm}^{-2}$ , the volume fraction was calculated to be  $\sim 10.4$  pct for the graphite anode and  $\sim 16.4$  pct for the industrial carbon anode. The fraction turned out to be more or less constant in the current density interval. However, the percentage of the nominal area of the horizontal part is 20 pct for both anodes (horizontal area/total area =  $0.785/3.925$ ). This implies that the current density on the horizontal part is  $\sim 50$  and  $\sim 80$  pct of the nominal current density for the graphite and industrial carbon anode, respectively. This difference is due to more active sites on the industrial carbon in comparison to the graphite which results in production of more bubbles. All results of gas fraction divided by nominal surface area for the different current densities are shown in Figure 15(b). Since the value is  $< 1$  it means that less gas was produced from the horizontal surface of the anode than expected correlated to the surface area. This could be explained by a great number of smaller bubbles were produced and detached faster from the vertical surface while big bubbles were slowly building up at the horizontal surface blocking more and more of the surface. Figure shows that value did not change much with current density which was surprising as it could be expected that the bubble-induced

convection should help removing bubbles at higher current densities relatively more for the horizontal surface than the vertical surface.

Since the values in Figure 15(b) are less than 1 it means that the corresponding number for the vertical surface area are greater than 1, and the current density on the vertical surface for the graphite is higher than corresponding current density for the industrial carbon. An effort was done to count the bubble on the vertical part but due to great number of bubbles detached from the vertical surface and big bubbles taking with smaller bubbles when detaching, it was difficult to observe any difference between the graphite and industrial anode. Additionally, a stream of small bubbles on the industrial carbon anode can be seen that in theory should reduce the frequency of the detaching bubbles on the vertical part.

#### D. Anode Effect

In Figures 16 and 18 linear sweep voltammograms for both anodes are presented. The videos are available in the electronic supplementary material (ESM 4 and ESM 5). In both figures the voltammograms were recorded without IR-compensation. Afterwards the curves were IR-compensated using the value of the ohmic resistance at OCP for the cell. Frames from selected parts of the sweep are shown together with the current to voltage data.

As can be seen in Figure 16 starting from OCP, the first increase in current density is observed around  $0.8 \text{ V}$ . The current increase was due to  $\text{CO}_2/\text{CO}$  gas evolution. The current oscillations arise from growth, coalescence and detachment of bubbles as could be seen from the video recording using a high-speed camera. In frame (1) is shown production of bubbles and their detachment during reaction at around  $1 \text{ A cm}^{-2}$ . Frame (2) represented the state of the anode just before the anode effect occurred. At cell voltage  $5.9 \text{ V}$  of the not-IR-compensated curve, the current suddenly decreased towards zero. The sudden decrease was attributed to the occurrence of the anode effect, forming a gas layer on the surface of the anode, frame (3) and (4). The bubble at the horizontal part of the anode was at its maximum size when the anode effect occurred. At the moment of anode effect bubble formation and bubble detachment stopped and the gas layer was formed at the surface completely covering the surface thus preventing contact between surface and electrolyte. The anode became completely non-wetted. The critical current density on the anode was exceeded, and the IR-compensated curve indicates that the potential of the anode is high enough to produce PFC according to reactions (1) and (2). Immediately after the decrease the current rose and decreased again whereupon it stayed unchanged with increasing voltage. The rise in current can be explained by the sudden increase in potential of the electrode when the current drops instantly to zero at anode effect, as seen from the IR-compensated curve. Some of the electrolyte that remained on the anode surface under the gas layer might have been oxidized during the abrupt potential increase of the anode. The layer was covering

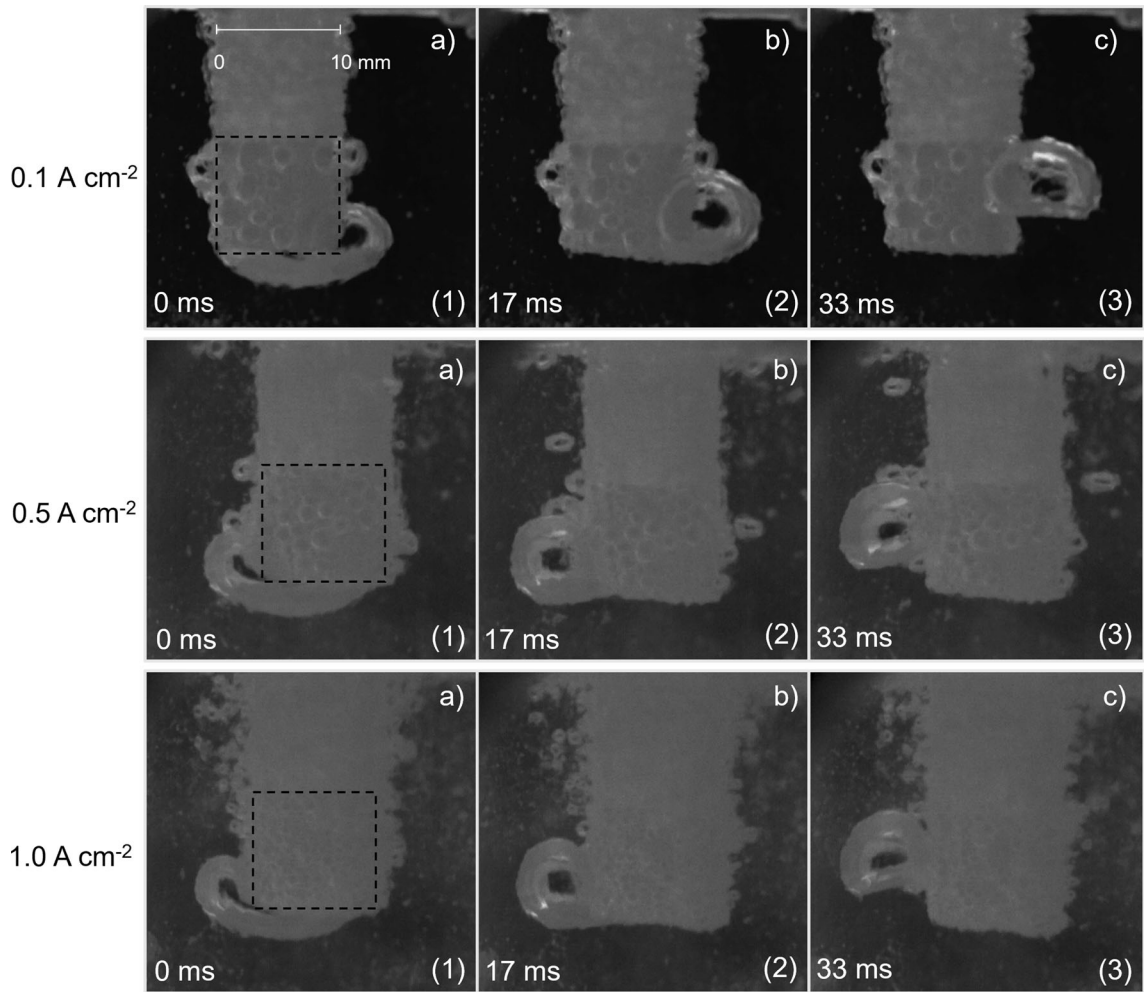


Fig. 14—Shielded rod graphite anode during electrolysis at different current densities, 0.1, 0.5 and 1.0 A cm<sup>-2</sup>, while (a) big bubble from the horizontal surface is sliding toward the anode edge, (b) big bubble is detaching from the anode edge and (c) big bubble is leaving the anode surface. The frame rate was 60 fps. Frame numbers are given in brackets. Timestamp of 0 ms is added to frame (1), by that, other frames are relative to the first frame. The anode surface is highlighted with a black dashed line in frame (1) together with a scale bar.

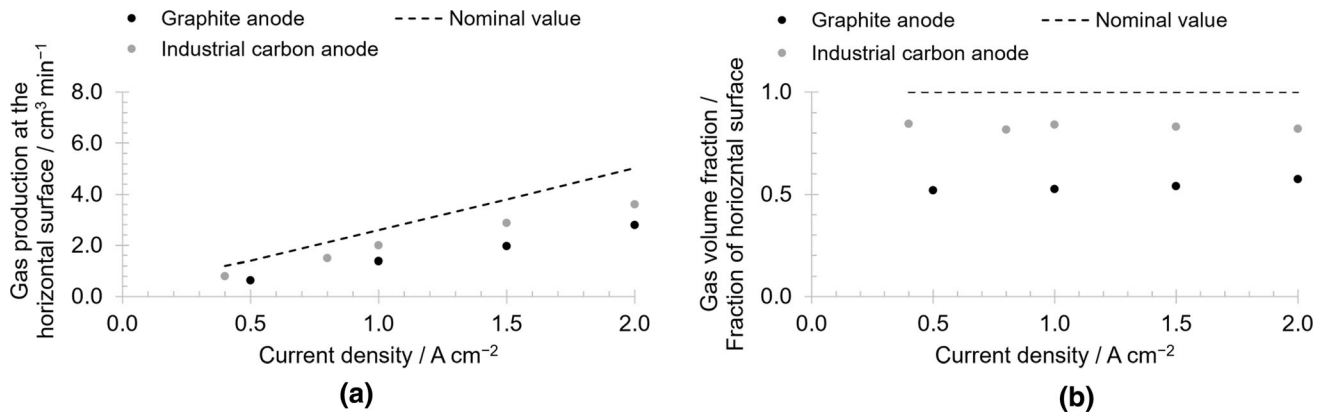


Fig. 15—Gas production on the horizontal surface for different current densities: (a) Gas volume rate, (b) Gas volume fraction.

the whole anode surface, and gas produced after the initiation anode effect was trapped inside the gas layer and was ended up at C/BN boundary, frame (5) and (6).

A principal sketch of the carbon anode before and after anode effect is shown in Figures 17(a) and (b), respectively. During the production PFC gas, the surface has been teflonised. Åsheim *et al.*<sup>[32]</sup> studied

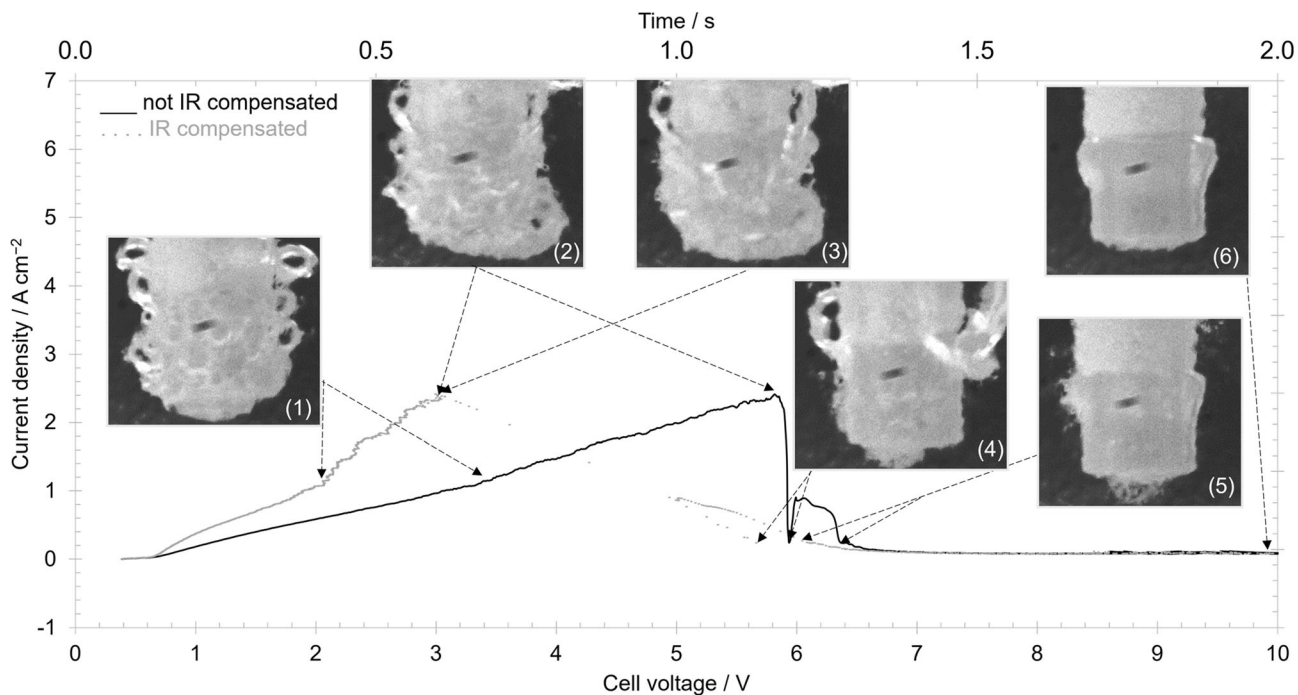


Fig. 16—Linear sweep voltammetry (LSV) curves for graphite anode with sweep rate of  $5 \text{ V s}^{-1}$  with corresponding frames from video recordings. Frames are numbered in display order, not in true time frames. Not IR and IR-compensated data are shown. Sampling frequency was 500 Hz. Timeline is only valid for not IR-compensated data.

wetting properties of the graphite using immersion/emersion technique and observed that anodes polarized to anode effect showed a consistent de-wetting which could confirm teflonisation of the anode surface. Haverkamp<sup>[33]</sup> studied fluorination of carbon anode using XPS and SEM and discovered fluorocarbon on the anode surface resulting from anode effect. The author concluded that a (C to F) film exist. As discussed earlier in 3.3.2., it seemed that the interfacial tension at carbon to electrolyte interface ( $\gamma_{si}$ ) is sufficiently small so that the electrolyte partly wets the carbon surface giving the bubbles a spherical shape, Figure 17a). After anode effect the gas layer at the carbon surface is believed to be mixture of CO/CO<sub>2</sub>/PFC gases, Figure 17b). Since chemically similar media require less energy to form an interface between them, the interfacial tension between a teflonised carbon surface (C to F) and CO/CO<sub>2</sub>/PFC gas layer ( $\gamma_{sg}$ ) is low and the gas layer is covering all the anode surface, Figure 17b). It appears that the (C to F) bond now have drastically increased the interfacial tension for the carbon electrolyte interface ( $\gamma_{si}$ ). The gas layer contributed to de-wetting of the anode. As observed the gas layer does not extend into the BN surface. This could be due to good wetting between electrolyte and BN which was also found by Åsheim *et al.*<sup>[32]</sup>.

A similar discussion can be applied for the anode effect on the industrial carbon anode, shown in Figure 18. Starting from OCP the first increase in current density also occurred at 0.8 V. However, the current density increased faster. In frame (1) are shown production and detachment of bubbles during reaction at

around  $1.5 \text{ A cm}^{-2}$ . In frame (2) is shown detachment of a big bubble from the horizontal surface prior to anode effect. The critical current density on the anode was exceeded, and the potential of the anode was high enough to produce PFC according to reactions (1) and (2), as can be seen from the IR-compensated curve. The decrease in current due to the onset anode effect is not abrupt as for the graphite, frame (3). From video recordings it can be observed that gas layer didn't spread as evenly and fast as for the graphite anode. Hence frame (4) still shows some gas bubble detachment. Similar phenomenon of rise in the current after initiation of the anode effect for the graphite was also observed here. The rise again can be explained by the sudden increase in potential of the electrode when the current drops towards zero at the onset of the anode affect and some of the electrolyte remaining under the gas layer might have been oxidized. Due to more porous surface of the industrial carbon anode, more electrolyte could be present beneath the gas layer on the anode surface leading to more gas production. The layer was covering the whole anode surface, and gas produced after the initiation anode effect was trapped inside the gas layer and was ended up at C/BN boundary but it does not stay trapped like in the case for graphite. The quantity of produced gas appears to be sufficient to overcome and break the layer to be detached, frame (5) and (6). The graphite anode has smoother, less porous and less complex surface than the industrial anode and the gas layer formed on the graphite anode appeared to be thicker, and more stable. The experiments were repeated five times for the same anode in the same



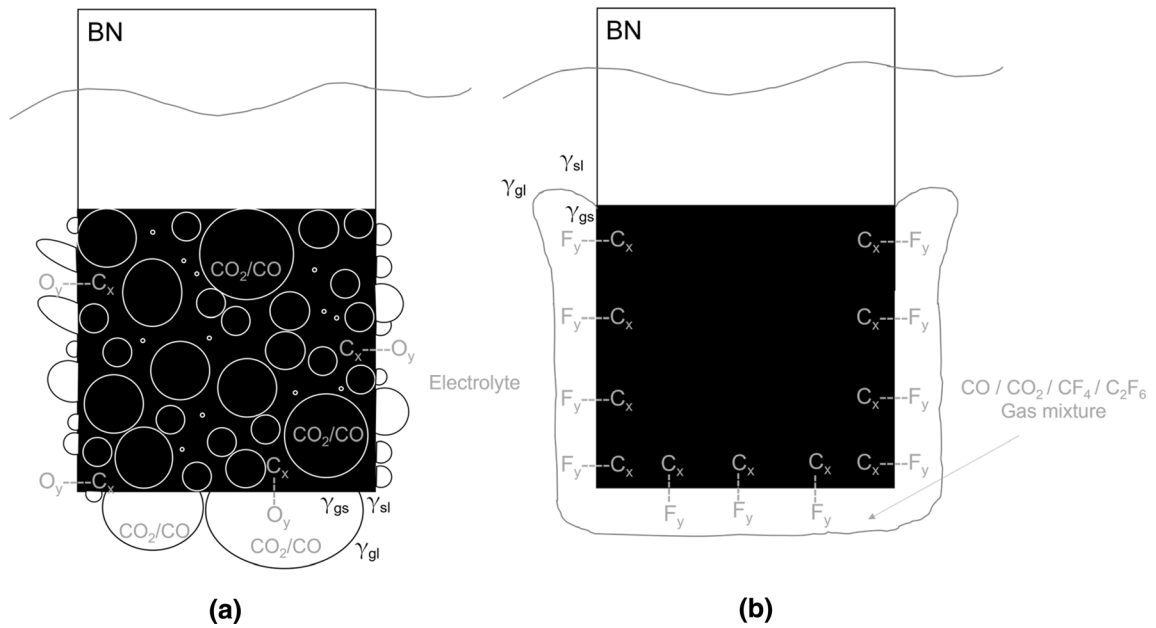


Fig. 17—Principal sketch of (a)  $\text{CO}_2/\text{CO}$  gas bubbles during the anode process for normal electrolysis and (b) after initiation of anode effect. The thickness of the perfluorocarbon containing gas layer is exaggerated for reasons of clarity.

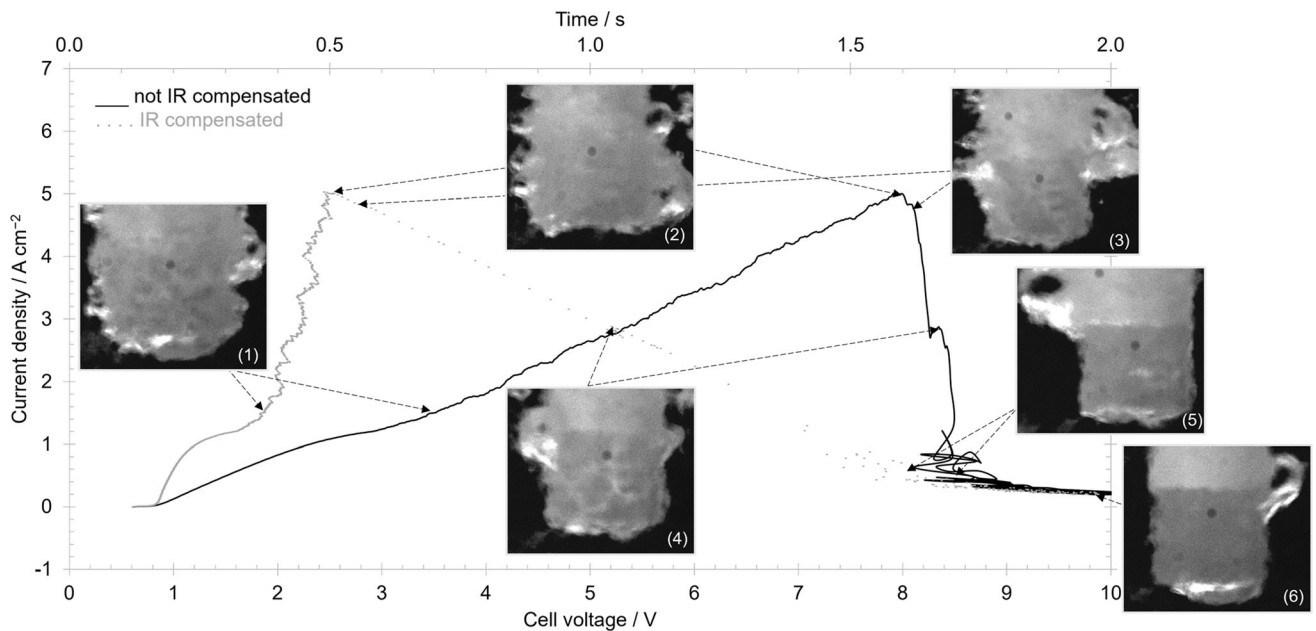


Fig. 18—Linear sweep voltammetry (LSV) curves for the industrial carbon anode with sweep rate of  $5 \text{ V s}^{-1}$  with corresponding frames from video recordings. Frames are numbered in display order, not in true time frames. Not IR and IR-compensated data are shown. Sampling frequency was 500 Hz. Timeline is only valid for not IR-compensated data.

crucible for a total six crucibles giving a total of approx. 30 sweeps. The anode effect always occurred on the graphite anode while on the industrial carbon, anode effect occurred only in approx. 60 pct of the sweeps.

In the voltage range above 8.5 V, distortion of the curve occurred for both anodes, although more pronounced in the case of the industrial carbon anode. This could be due to instrument limitation. The voltage

range limitation is 0 to 10 V. When current drops suddenly due to the onset on the anode effect, the voltage increases significantly from 3 to 6 V in the case of the graphite anode and from 2.5 to 8.5 V in the case of the industrial carbon anode (this can be seen from IR-compensated curves), and probably due to short term overloading of the instrument curves gets distorted.

## IV. CONCLUSIONS

More bubbles were nucleated on the industrial carbon anode than on the graphite anode for the same current density. The higher number of bubbles was due to more active sites on the industrial carbon confirmed by CT analysis which showed that the industrial carbon has much larger aggregates with more pores, cracks and impurities in comparison to the graphite. On both horizontal and vertical surfaces the smaller bubbles coalesced into bigger bubbles. The time related to the process of coalescence for both anodes was found to be in the interval 16 to 24 ms and independent of the current density. The bubbles on the vertical surface detached through a preceding coalescence process while the bubbles on the horizontal surface coalesced and went off as a one big bubble. However, on the industrial carbon more bubbles were produced. For both anode materials the diameter of detached bubbles decreased with increasing current density. Bubbles from the vertical surface are found to be similar in diameter for both anodes for the same current density. Big bubbles detaching from the horizontal surface have also similar diameter for the same current density but the detachment frequency of big bubbles was higher for the industrial carbon. This was explained by the higher current density found on the horizontal surface of the industrial carbon anode compared to the graphite anode. For current densities  $> 1.0 \text{ A cm}^{-2}$ , some smaller bubbles were produced alongside the big bubbles at the horizontal surface for the industrial carbon anode. On increased currents anode effect occurred on both anodes, the current being lower for the graphite anode at the onset. The video recordings and the electrochemical measurements showed more abrupt initiation of the anode effect on the graphite. A PFC-containing gas layer was formed around the anode and the layer appeared to be thicker and more stable on the graphite anode than on the industrial anode.

## CONFLICT OF INTEREST

Conflict of interest On behalf of all authors, the corresponding author states that there is no conflict of interest.

## FUNDING

Open access funding provided by NTNU Norwegian University of Science and Technology (incl St. Olavs Hospital - Trondheim University Hospital).

## OPEN ACCESS

This article is licensed under a Creative Commons Attribution 4.0 International License, which permits use, sharing, adaptation, distribution and reproduction in any medium or format, as long as you give appropriate credit to the original author(s) and the source,

provide a link to the Creative Commons licence, and indicate if changes were made. The images or other third party material in this article are included in the article's Creative Commons licence, unless indicated otherwise in a credit line to the material. If material is not included in the article's Creative Commons licence and your intended use is not permitted by statutory regulation or exceeds the permitted use, you will need to obtain permission directly from the copyright holder. To view a copy of this licence, visit <http://creativecommons.org/licenses/by/4.0/>.

## SUPPLEMENTARY INFORMATION

The online version contains supplementary material available at <https://doi.org/10.1007/s11663-022-02583-6>.

## REFERENCES

1. Z. Zhao, Z. Wang, B. Gao, Y. Feng, Z. Shi, and X. Hu: *Light Metals*, Springer, Cham, 2015, pp. 801–06.
2. Y. Huang, Z. Wang, Y. Yang, B. Gao, Z. Shi, and Hu: *Metals*, 2018, vol. 8, p. 806.
3. D. Kasherman and M. Skyllas-Kazacos: *J. Appl. Electrochem.*, 1991, vol. 21, pp. 716–20.
4. R.J. Thorne, C. Sommerseth, A.P. Ratvik, S. Rorvik, E. Sandnes, L. Lossius, H. Linga, and A. Svensson: *J. Electrochem. Soc.*, 2015, vol. 162, pp. E296–306.
5. R.J. Thorne, C. Sommerseth, A.M. Svensson, E. Sandnes, L.P. Lossius, H. Linga, and A.P. Ratvik: *Light Metals*, Wiley, Hoboken, NJ, 2014, pp. 1213–17.
6. R.J. Thorne, C. Sommerseth, E. Sandnes, O. Kjos, T.A. Aarhaug, L.P. Lossius, H. Linga, and A.P. Ratvik: *Light Metals*, Springer, Berlin, 2013, pp. 1207–11.
7. A. Tabereaux: *JOM*, 1994, vol. 46, pp. 30–34.
8. J. Thonstad, F. Nordmo, and K. Vee: *Electrochim. Acta*, 1973, vol. 18(1), pp. 27–32.
9. J. Thonstad, F. Nordmo, and J.K. Rødseth: *Electrochim. Acta*, 1974, vol. 19(11), pp. 761–69.
10. F. Nordmo and J. Thonstad: *Electrochim. Acta*, 1984, vol. 29(9), pp. 1257–62.
11. J. Thonstad, S. Rolseth, and R. Keller: *Light Metals*, Springer, Cham, 2013, pp. 883–85.
12. Zhu, H. and D. Sadoway: *Light Metals: Proceedings of Sessions, TMS Annual Meeting (Warrendale, Pennsylvania)*, 2000, p. 257–263.
13. H. Zhu: *ECS Proceedings Volumes*, 2002, vol. 2002–19(1), pp. 411–18.
14. A.T. Tabereaux, N.E. Richards, and C.E. Satchel: *Light Metals*, TMS, Warrendale, 1995, pp. 325–33.
15. N. Stanic, A.M. Martinez, K.E. Einarsrud, and E. Sandnes: *Metals*, 2021, vol. 11, p. 24.
16. N. Stanic and E. Sandnes: *Mater. Proc.*, 2021, vol. 3(1), p. 8.
17. SignalLab. SigView Spectrum Analyzer. 2021 [cited 2021]. <https://www.sigview.com/>.
18. ICDD PDF-4 Phase Identification & Quantitation, 2021, International Centre Diffraction Data Newtown Square, PA. Accessed 27 Sept 2021.
19. H. Villarraga-Gómez and S. Smith: *Precis. Eng.*, 2020, vol. 66, pp. 445–56.
20. D. Picard, H. Alamdari, D. Ziegler, P.-O. St-Arnaud, and M. Fafard: *Light Metals*, Springer, Cham, 2011, pp. 973–78.
21. A. Vlahov: *Geolog. Balcan.*, 2021, vol. 50, pp. 11–35.
22. P. Ouzilleau, A.E. Gheribi, and P. Chartrand: *Electrochim. Acta*, 2018, vol. 259, pp. 916–29.
23. J. Thonstad: *J. Electrochem. Soc.*, 1965, vol. 111(8), pp. 959–65.

24. P. Droßbach: *Z. Elektrochem. Angew. Phys. Chem.*, 1936, vol. 42(2), pp. 65–70.
25. N. Stanic, I. Jevremovic, A.M. Martinez, and E. Sandnes: *Metall. Mater. Trans. B.*, 2020, vol. 51B(3), pp. 1243–53.
26. R.J. Thorne, C. Sommerseth, A.P. Ratvik, S. Rorvik, E. Sandnes, L.P. Lossius, H. Linga, and A. Svensson: *J. Electrochem. Soc.*, 2015, vol. 162(8), pp. E104–14.
27. J. Holbrough, J. Campbell, F. Meldrum, and H. Christenson: *Cryst. Growth Des.*, 2012, vol. 12, pp. 750–55.
28. D.E. Westerheide and J.W. Westwater: *AIChE J*, 1961, vol. 7(3), pp. 357–62.
29. K. Obata and F. Abdi: *Sustain. Energy Fuels*, 2021, vol. 5, p. 1.
30. L. Cassayre, T. Utigard, and S. Bouvet: *JOM*, 2002, vol. 54(5), pp. 41–45.
31. L. Cassayre, G. Plascencia, T. Marin, S. Fan, and T. Utigard: *Light Metals*, TMS, Warrendale, 2006, pp. 379–83.
32. H. Åsheim, I.A. Eidsvaag, A. Solheim, H. Gudbrandsen, G.M. Haarberg, and E. Sandnes: *Light Metals*, Springer, Cham, 2020, pp. 608–19.
33. R.G. Haverkamp: *J. Mater. Sci.*, 2012, vol. 47(3), pp. 1262–67.

**Publisher's Note** Springer Nature remains neutral with regard to jurisdictional claims in published maps and institutional affiliations.